LAWRENCE
LIVERMORE
NATIONAL
LABORATORY

LLNL-JRNL-801713

Hotspot conditions achieved in Inertial Confinement Fusion Experiments on the National Ignition Facility

P. K. Patel, P. T. Springer, C. R. Weber, L. C. Jarrott, O. A. Hurricane, B. Bachmann, K. L. B aker, L. Berzak Hopkins, D. A. Callahan, D. Casey, C. Cerjan, D. S. Clark, E. Dewald, L. Divol, T. Doeppner, J. Field, D. Fittinghof, J. Gaffney, V. Geppert-Kleinrath, G. Grim, E. Hartouni, R. Hatarik, D. Hinkel, M. Hohenberger, K. Humbird, N. Izumi, O. Jones, S. Khan, A. Kritcher, M. Kruse, O. L. Landen, S. Le Pape, T. Ma, S. MacLaren, A. MacPhee, L. Masse, J. L. Milovich, R. Nora, A. Pak, J. L. Peterson, J. Ralph, H. Robey, J. D. Salmonson, V. A. Smalyuk, B. K. Spears, C. Thomas, P. L. Volegov, A. Zylstra, M. J. Edwards

January 17, 2020

Physics of Plasmas

Disclaimer

LLNL-JRNL-801713

Hotspot conditions achieved in Inertial Confinement Fusion Experiments on the National Ignition Facility

P. K. Patel,[1, a)] P. T. Springer,[1] C. R. Weber,[1] L. C. Jarrott,[1] O. A. Hurricane,[1] B. Bachmann,[1] K. L. Baker,[1] L. F. Berzak Hopkins,[1] D. A. Callahan,[1] D. T. Casey,[1] C. J. Cerjan,[1] D. S. Clark,[1] E. L. Dewald,[1] L. Divol,[1] T. Döppner,[1] J. E. Field,[1] D. Fittinghoff,[1] J. Gaffney,[1] V. Geppert-Kleinrath,[2] G. P. Grim,[1] E. P. Hartouni,[1] R. Hatarik,[1] D. E. Hinkel,[1] M. Hohenberger,[1] K. Humbird,[1] N. Izumi,[1] O. S. Jones,[1] S. F. Khan,[1] A. L. Kritcher,[1] M. Kruse,[1] O. L. Landen,[1] S. Le Pape,[1, 3] T. Ma,[1] S. A. MacLaren,[1] A. G. MacPhee,[1] L. P. Masse,[1] N. B. Meezan,[1] J. L. Milovich,[1] R. Nora,[1] A. Pak,[1] J. L. Peterson,[1] J. Ralph,[1] H. F. Robey,[1] J. D. Salmonson,[1] V. A. Smalyuk,[1] B. K. Spears,[1] C. A. Thomas,[4] P. L. Volegov,[2] A. Zylstra,[1] and M. J. Edwards[1]

[1)] *Lawrence Livermore National Laboratory, Livermore, CA 94551, USA*

[2)] *Los Alamos National Laboratory, Los Alamos, NM 87545, USA*

[3)] *Laboratoire pour L'Utilisation des Lasers Intenses, Ecole Polytechnique, 91128 Palaiseau cedex, France*

[4)] *Laboratory for Laser Energetics, University of Rochester, Rochester, NY 14620, USA*

(Dated: 15 July 2020)

We describe the overall performance of the major indirect-drive inertial confinement fusion (ICF) campaigns executed at the National Ignition Facility (NIF). With respect to the proximity to ignition we can describe the performance of current experiments both in terms of no-burn ignition metrics (metrics based on the hydrodynamic performance of targets in the absence of alpha-particle heating), and in terms of the thermodynamic properties of the hotspot and dense fuel at stagnation—in particular the hotspot pressure, temperature, and areal density. We describe a simple 1D isobaric model to derive these quantities from experimental observables, and examine where current experiments lie with respect to the conditions required for ignition.

I. INTRODUCTION

The indirect-drive approach to inertial confinement fusion (ICF) aims to achieve ignition through the spherical compression of a deuterium-tritium (DT) filled capsule driven by x-rays generated from the laser irradiation of a high-Z hohlraum.[1,2] Since the beginning of the experimental program following the completion of the National Ignition Facility (NIF) in 2009 considerable progress has been made both in our understanding of the implosion behavior and in the overall performance attained. The highest yield to date has increased by more than 20x from the end of the first campaign in 2012, reaching 2.0×10^{16} neutrons, or 55 kJ of fusion energy. Whilst the total yield produced by an implosion provides an essentially unambiguous yardstick for whether or not the implosion has ignited, given the implicit threshold behavior of ignition the total yield is not the best quantitative measure of the proximity, or gap, to ignition. For this assessment, other metrics based on power balance in the hotspot, or the yield amplification from equivalent *no-burn* implosions, i.e., hydrodynamically equivalent implosions with alpha-heating artificially turned off, can be more meaningful.

The purpose of this paper is to summarize the overall performance of DT-layered experiments on the NIF in terms of the hotspot conditions produced at stagnation and the implications for the proximity to ignition. We begin with a brief introduction to the major implosion campaigns. In Section II we describe the method used to infer no-burn ignition metrics and yield amplification. In Section III we describe a static hotspot model used to infer hotspot properties including pressure, temperature and areal density. Finally, in Section IV we employ a dynamic model to relate these inferred hotspot properties to those required for ignition.

We first summarize the performance of the four major campaigns performed on NIF since 2009. Two of these used a plastic (CH) ablator, and the other two a high-density-carbon (HDC) ablator. Figure 1 shows the overall performance of the experiments in these campaigns in terms of the measured neutron yield and down-scattered ratio (DSR). The DSR is the ratio of observed neutrons with energies between 10-12 MeV over 13-15 MeV and is an approximate measure of the total DT fuel areal density (ρR_{tot} [g/cm^2] $\approx 21 \times DSR$).[3] In this parameter space contours can be drawn of constant yield amplification for a given DT fuel mass (the method for calculating these contours is described in Section II). For each level of yield amplification shown the lower line corresponds to a DT fuel mass of 138 μg, the typical value used in the HDC designs and the upper line corresponds to a DT fuel mass of 180 μg, typically used in the CH designs. The original CH 4-shock low-foot design (CH LF), with a design adiabat of $\alpha \sim 1.6$, achieved relatively high values of DSR in the range DSR $\sim$ 4–6%, equivalent to fuel areal densities of $\rho R_{tot} \sim$ 0.8–1.2 g/cm^2, but the max-

[a)] Electronic mail: patel9@llnl.gov

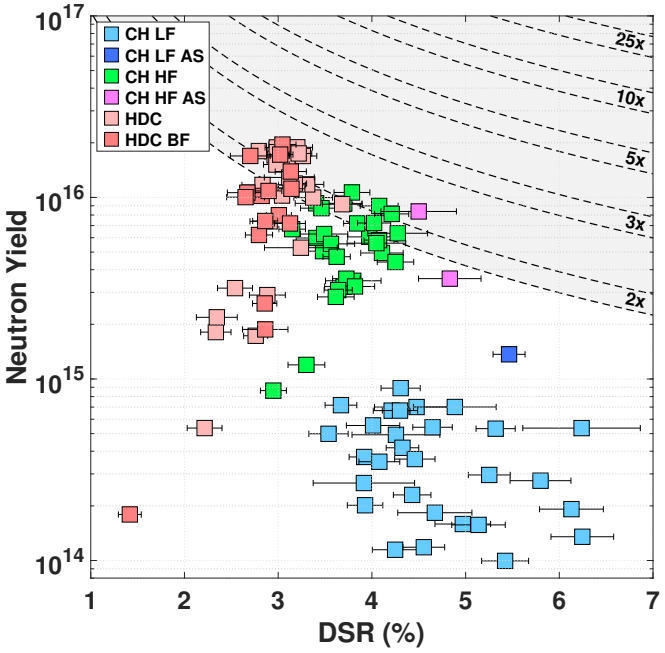

FIG. 1. Performance of DT implosion experiments in terms of total neutron yield and neutron down-scattered ratio. Dotted lines represent contours of yield amplification due to alpha-particle self-heating. For each level of yield amplification the lower line corresponds to DT fuel mass generally used in HDC ablator experiments and the upper line corresponds to DT fuel mass used in CH ablator experiments.

imum yield was limited to 9×10^{14} neutrons, in large part because of high levels of radiation drive asymmetry, hydro-instability seeded by the capsule support tent, and high-Z mix in the hotspot.[4,5]

The CH high-foot implosion (CH HF) used a modified 3-shock drive with a stronger first shock designed to reduce ablation-front Rayleigh-Taylor instability to produce a hydrodynamically more stable implosion at the cost of higher adiabat ($\alpha \sim 2.3$) and lower theoretical fuel compression. Performance did indeed dramatically improve with neutron yields increasing a factor of 10× over the CH LF design to 1×10^{16} neutrons.[6,7] As expected the higher adiabat resulted in a lower DSR of ∼ 3.2–4.2%, or $\rho R_{tot} \sim 0.64$–0.84 g/cm^2. As can be seen in Fig. 1 the best performing high-foot implosions achieved for the first time a doubling of fusion yield due to alpha-particle self-heating. Ultimately, the performance at the highest implosion velocities was again limited by 3D drive asymmetries and the tent perturbation.

To test whether further improvements could be realized by maintaining comparable levels of ablative stabilization, but increasing the areal density of the DT fuel, so-called "adiabat-shaped" versions of the CH LF and CH HF drives were developed. These designs utilized a decaying first shock in order to combine low ablation-front hydro-instability with low adiabat and consequently high theoretical fuel compression.[8] For the adiabat-shaped version of the CH LF (CH LF AS) the improvement in hydro-stability was verified in hydrodynamic growth radiography (HGR) experiments[9] and a subsequent DT implosion[10] produced a neutron yield of 1.4×10^{15}—an increase over similar companion CH LF shots, though still lower than companion CH HF shots. Two DT implosion experiments using the adiabat-shaped high-foot pulse (CH HF AS) resulted in increased DSR but similar neutron yields to comparable CH HF shots, suggesting that the benefit of higher DSR was offset by other factors such as worsening 3D shape at the higher convergence.

At that time a persistent problem in all of the campaigns that used high-gas-fill hohlraums (He gas densities of 0.96–1.6 mg/cc) was the low efficiency with which laser energy was being converted to x-ray drive energy. Typically, 15% of the laser light entering the hohlraum underwent backscatter due to laser-plasma instabilities (LPI), and a further 15–25% deficit in effectively coupled drive energy was unexplained, resulting in an overall hohlraum efficiency of just 60–70%.[11] This in turn exacerbated the difficulty in achieving the uniformity of drive needed for a symmetric implosion.[12] A new design was developed to mitigate these problems primarily by reducing the hohlraum gas-fill density to 0.03–0.3 mg/cc and using a high-density carbon (HDC) ablator instead of CH. Being higher density the HDC ablator permitted the use of a thinner shell, and hence, shorter drive duration needed to permit the reduction in gas-fill density.[13] The 3-shock HDC design, operating at a design adiabat of $\alpha \sim 2.5$, achieved a 2× improvement in neutron yield over the CH HF, to 1.89×10^{16} corresponding to 53 kJ of fusion energy output.[14,15] A second HDC ablator design, termed the "Big Foot" (HDC BF), was developed to operate at a higher design adiabat of $\alpha \sim 4$, as well as incorporate other changes to the laser and target geometry intended to make the hohlraum symmetry control better and more predictable.[16] The HDC BF campaign achieved a similar level of overall performance as the HDC, reaching a peak neutron yield of 1.96×10^{16} or 55 kJ fusion energy.[17] Despite the different design adiabats both types of implosion achieved a similar DSR of $\sim 3.2\%$ ($\rho R_{tot} \sim 0.64$ g/cm^2). The reason for this is not well understood, though current modeling suggests that different levels of implosion stability may have led to similar DSRs in the two designs despite the different design adiabats. Current designs are focusing on further improving upon the high performing HDC designs by increasing the capsule size to couple more energy to the implosion.[18,19]

In terms of understanding our proximity to ignition it useful to look not just at the absolute yield, but at the degree of alpha-heating that boosts or amplifies the yield, ultimately leading to the runaway process of ignition. This is the subject of the next Section.

II. YIELD AMPLIFICATION AND IGNITION PARAMETERS

Analytic and computational studies have shown that the amplification in yield from alpha-heating can be expressed by a single metric that is a function of the neutron yield, the fuel areal density, and the fuel mass at stagnation. Spears *et al.*[20–22] developed the experimentally observable ignition threshold factor (ITFX) based on a large ensemble of 2D radiation-hydrodynamics simulations of the original CH low-foot (CH LF) design.[23] ITFX is defined by,

$$ITFX_{n\alpha,\alpha} = \left(\frac{170}{M_{DT}}\right)\left(\frac{Y^{13\text{-}15}_{n\alpha,\alpha}}{4\text{E}15}\right)\left(\frac{DSR_{n\alpha,\alpha}}{0.067}\right)^{2.1} \quad (1)$$

where M_{DT} is the total DT fuel mass in μg (170 μg for this design), and $Y^{13\text{-}15}$ is the measured neutron yield between 13 to 15 MeV. In Eqn. 1 ITFX is defined both for implosions where alpha-particle deposition is included, $ITFX_\alpha$, and for where alpha-particle deposition is artificially turned off in the simulation, $ITFX_{n\alpha}$. The metric is normalized such that $ITFX_{n\alpha} = 1$ for this design when the yield $Y^{DT} = 1$ MJ. Y^{DT} is the total neutron yield from D-T fusion reactions, over all energies. As is evident from Eqn. 1 the neutron yield corresponding to an $ITFX_{n\alpha} = 1$ is not unique for all target designs, but will vary with the fuel mass and DSR. Whilst the absolute yield is not unique across target designs, the yield amplification due to alpha-particle self-heating, $Y^{\rm DT}_\alpha/Y^{\rm DT}_{n\alpha}$, is found to correlate strongly with $ITFX$ independent of target design. Figure 2 shows the relationship between the yield amplification with both $ITFX_\alpha$ and $ITFX_{n\alpha}$ for a set of 1D and 2D postshot simulations spanning a variety of target designs and capsule scales, including CH LF, CH HF, HDC, and HDC BF experiments. The simulations include a variety of sources of asymmetry including low-mode radiation drive asymmetries, and in some cases high-mode capsule surface roughness and tent and fill-tube models.[12,24] The solid lines in Fig. 2 are best fits to the simulation database and are given by,

$$Y^{\rm DT}_\alpha/Y^{\rm DT}_{n\alpha} = \exp(0.9ITFX^{0.47}_\alpha) \quad (2)$$

and

$$ITFX_{n\alpha} = ITFX_\alpha \times \exp(-0.9ITFX^{0.47}_\alpha + 0.007ITFX^{1.65}_\alpha) \quad (3)$$

The fits are generally valid up to yield amplifications of approximately 20-30x where the increased fusion yield predominately originates from self-heating and ignition of the hotspot. As the thermonuclear burn begins to propagate into the dense fuel surrounding the hotspot one can expect a much higher variability in the total yield and yield amplification.[25]

An alternative ignition parameter based on the Lawson criterion is given by Betti *et al.*[26–28],

$$\chi_{n\alpha} = (\rho R_{n\alpha})^{0.61}\left(\frac{0.12Y^{16}_{n\alpha}}{M_{stag}}\right)^{0.34} \quad (4)$$

where ρR is the neutron-weighted fuel areal density, Y^{16} is the total neutron yield in units of 10^{16} neutrons, and M_{stag} is the stagnated DT mass in mg. The two metrics have a very similar form and are approximately related by $\chi_{n\alpha} \approx ITFX^{0.34}_{n\alpha}$. This provides a convenient method to infer the approximate value of $\chi_{n\alpha}$ from the experimentally measured value of $ITFX_\alpha$ and Eqn. 3.

Using the experimentally measured $ITFX_\alpha$ and the fits in Eqns. 2 and 3 we infer $ITFX_{n\alpha}$ and yield amplification for all of the HDC and BF experiments and plot in Fig. 3. The highest value reached to date is $ITFX_{n\alpha} = 0.43$, equivalent to $\chi_{n\alpha} \approx 0.75$, which corresponds to a yield amplification $Y^{\rm DT}_\alpha/Y^{\rm DT}_{n\alpha} = 2.55 \pm 0.17$. We see that at the present value of $\chi_{n\alpha}$ the yield amplification begins to steepen rapidly, so that small increases in $\chi_{n\alpha}$ would be expected to result in rapidly increasing levels of yield amplification and absolute yield. In Fig. 4 we plot the measured experimental yields vs. the ignition parameter. The solid and dotted lines are the expected yields for implosions with and without alpha-heating, respectively, for the case of $M_{DT} = 138$ μg and $DSR_{n\alpha} = 3.2$, which are representative of the majority of the shots in these campaigns. In both Figs. 3 and 4 one can see the signature of the onset of hotspot ignition by the distinct changes in curvature, or rates of increase in yield amplification and absolute yield, at $\chi_{n\alpha} \approx 0.90$, a value that is $\sim 20\%$ beyond the highest achieved to date. Conceptually, there are two paths for increasing $\chi_{n\alpha}$—either to increase the stagnation pressure by improving the implosion quality at a fixed scale, or to increase the scale whilst maintaining constant pressure, effectively increasing the confinement time. A particular form of scaling is *hydro-equivalent* scaling, in which all spatial and temporal dimensions are increased by some factor S. In this case it has been shown by Nora *et al.*[29] that the ignition parameter scales as $\chi_{n\alpha} \sim S^{1.1}$. Thus, in the absence of further improvements to the stagnation pressure, the scale would need to increase by $S \sim 20\%$ to reach a $\chi_{n\alpha}$ of 0.90, and by $S \sim 30\%$ to reach a $\chi_{n\alpha}$ of 1.0.

III. STAGNATION CONDITIONS

While the ignition parameters discussed in the previous section provide a quantitative measure of the proximity to ignition in terms of no-burn neutron yield and total fuel ρR one can gain much more physical insight by studying the thermodynamic conditions in the hotspot at stagnation. We use a 1D static model to infer the hotspot conditions from experimental measurements. Whilst this is a highly simplified model we can test it with synthetic data from multi-D simulations to quantify how well it

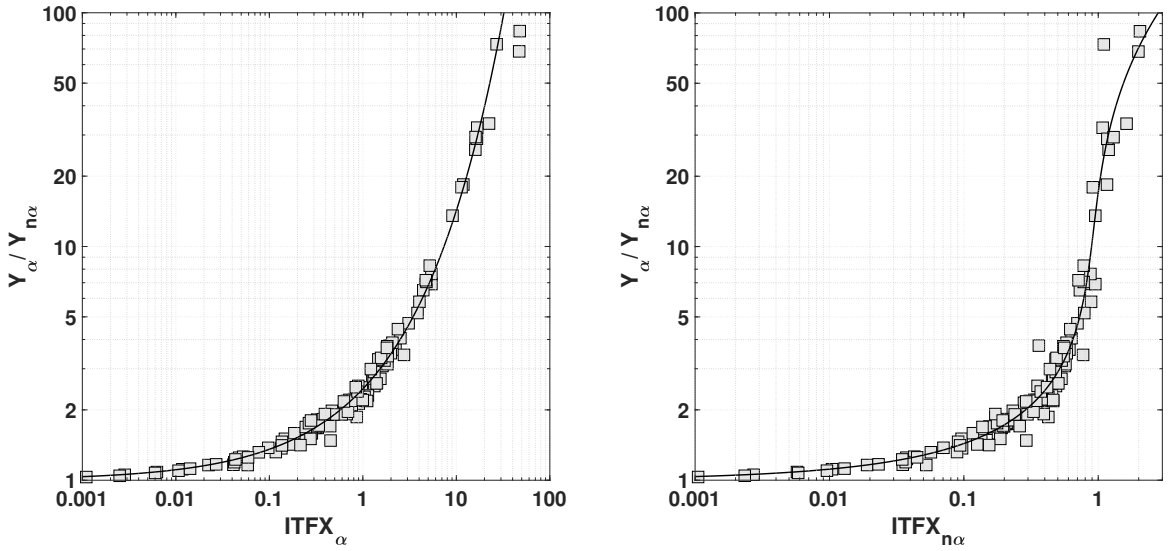

FIG. 2. Yield amplification due to alpha-heating as a function of $ITFX_\alpha$ (left), and $ITFX_{n\alpha}$ (right), for a suite of 1D and 2D postshot simulations of CH LF, CH HF, HDC, and HDC BF target experiments on the NIF. Solid lines represent best fits to the simulation points.

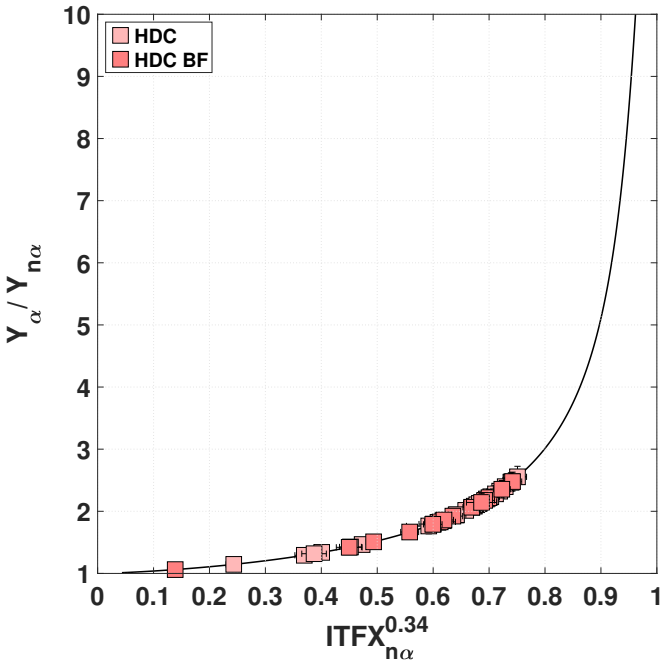

FIG. 3. Yield amplification vs. $ITFX_{n\alpha}^{0.34}$ for HDC and HDC BF designs, where $ITFX_{n\alpha}^{0.34} \approx \chi_{n\alpha}$. The solid line is from Eqns. 2 and 3. The highest value of $\chi_{n\alpha}$ reached to date is $\chi_{n\alpha} \approx 0.75$, corresponding to a yield amplification of 2.55 ± 0.17.

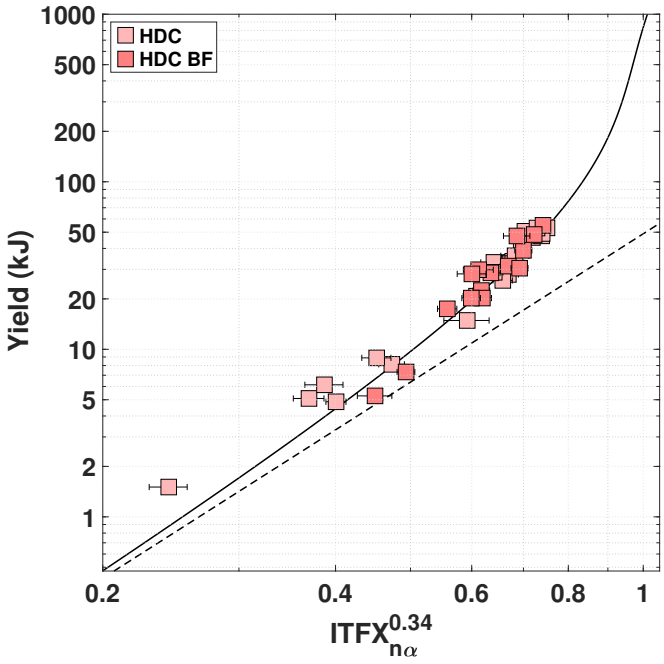

FIG. 4. Yield vs. $ITFX_{n\alpha}^{0.34}$ for HDC and HDC BF designs. The solid line is Eqn. 1 for $DSR_{n\alpha} = 3.2$. The dotted line is the equivalent yield in the case of no alpha-deposition.

approximates realistic implosions for the parameters of interest. The hotspot is approximated to be isobaric and have a temperature profile determined by thermal conduction within the hotspot.[30,31] We further assume the electrons and ions to be in thermal equilibrium with each other. The solution of the heat flow equation in this case has the approximate form,

$$T(r) = T_o \left(1 - \left(\frac{r}{R_o}\right)^2\right)^{\frac{1}{1+\beta}} \tag{5}$$

where T_o is the central temperature, R_o is the radius of the hotspot boundary, and β is the temperature exponent of the thermal conductivity, $K \propto T^\beta$.

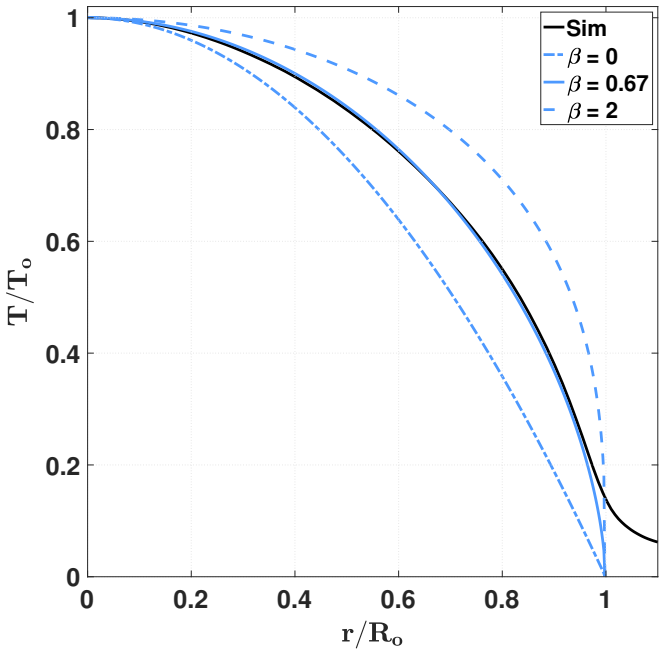

FIG. 5. Hotspot temperature profiles from Eqn. 5 for different values of the parameter β. The black line is the temperature profile at bangtime from a 1D simulation. The best agreement is obtained for a value of $\beta = 0.67$.

Figure 5 compares normalized temperature profiles for different values of β with a profile taken at the time of peak neutron production (bangtime) from a 1D simulation of an HDC implosion using the radiation-hydrodynamics code HYDRA. The best agreement is obtained for a value of $\beta = 0.67$. This is lower than the value $\beta = 2.5$ from classical Spitzer conductivity, or $\beta = 2.0$ from a fit to the Sesame database for a DT plasma. Partly, this is expected given the approximate form of Eqn. 5—a more complete solution is given in Betti *et al.*[32]. Additionally, other physical processes included in the full simulation will play a role in establishing the actual temperature profile. In order to best match the simulation we use the value $\beta = 0.67$ in the model.

For a hotspot pressure P the density profile is given by the ideal gas law,

$$\rho(r) = 1.3P/T(r) \tag{6}$$

where ρ is in g/cm^2, P is in Gbar, and T is in keV. The neutron yield per unit radius is

$$\frac{dY_n(r)}{dr} = 4\pi f_D f_T \frac{N_A^2}{A_{DT}^2}\rho(r)^2\sigma_{DT}(T(r))\tau_{BW}r^2 \tag{7}$$

where f_D and f_T are the deuterium and tritium fractions, respectively, A_{DT} is the average DT atomic mass, N_A is Avogadro's number, σ_{DT} is the DT fusion reactivity rate, and the integral over time is approximated by multiplying by the burnwidth τ_{BW}. The neutron-weighted ion temperature is then,

$$\langle T_i\rangle_n = \frac{1}{Y_n}\int T(r)\frac{dY_n(r)}{dr}\,dr \tag{8}$$

The temperature is usually obtained from the variance of the Doppler-broadened DT neutron spectral peak at 14 MeV.[33] On the NIF this is measured using several neutron-time-of-flight (NTOF) detectors arrayed around the target chamber.[34] However, the DT neutron peak can be broadened not just by thermal ion motion but also by the presence of residual velocity flow, or residual kinetic energy (RKE), in the hotspot resulting from incomplete conversion of kinetic to thermal energy during burn.[35,36]. In this case the variance of the DT neutron peak corresponds to an apparent temperature, T_{app}, that is the sum of the neutron-weighted thermal ion temperature, $\langle T_i\rangle_n$, and the neutron-weighted bulk fluid velocity variance, $\langle\sigma_v^2\rangle_n$, along the detector line-of-sight,

$$T_{app} = \langle T_i\rangle_n + (m_D + m_T)\langle\sigma_v^2\rangle_n \tag{9}$$

Experiments performed in the high-foot campaign gave measured NTOF T_{app} temperatures systematically higher than that expected from both theory and detailed postshot simulations, often by as much as $\Delta T \sim 1$ keV.[12,37] Experiments in low-gas fill hohlraums (HDC and HDC BF campaigns) at lower convergence and with improved radiation drive symmetry produced measured T_{app} temperatures more consistent with expectation. This suggested that the high-foot implosions may have had higher levels of RKE and hence T_{app} temperatures significantly higher than the thermal temperatures.[35,38]

An alternate method for measuring thermal temperature—one not affected by residual hotspot flows—was developed by Jarrott *et al.*[39,40] The method was to use measurements of the high-energy x-ray continuum spectrum from the hotspot to infer the thermal *electron* temperature. Electron and ion temperature measurements can differ, however, due to two possible effects. The first is from any difference in their equilibrium thermal temperatures. At early time the shock traversing the initial central gas preferentially heats the ions. As the hotspot is compressed the ions and electrons rapidly equilibrate and simulations predict that for the majority of the burn they are within a few percent of each other. At high levels of alpha-heating they can depart again in the opposite direction as alpha-particles preferentially heat the electrons. The second effect arises from the fact that there is a temperature distribution within the hotspot and the single value of temperature that we infer is that distribution weighted by the particles being measured, i.e., neutrons for ion temperature, and x-rays for electron temperature. Whereas the neutron emission scales with temperature, the x-ray emission scales with both temperature and photon energy, $h\nu$, as $\exp(-h\nu/T_e)$, and hence the temperature inferred from the x-ray continuum slope depends on the photon energies being measured. If $\epsilon_{h\nu}$ is the x-ray emission from the hotspot then the x-ray

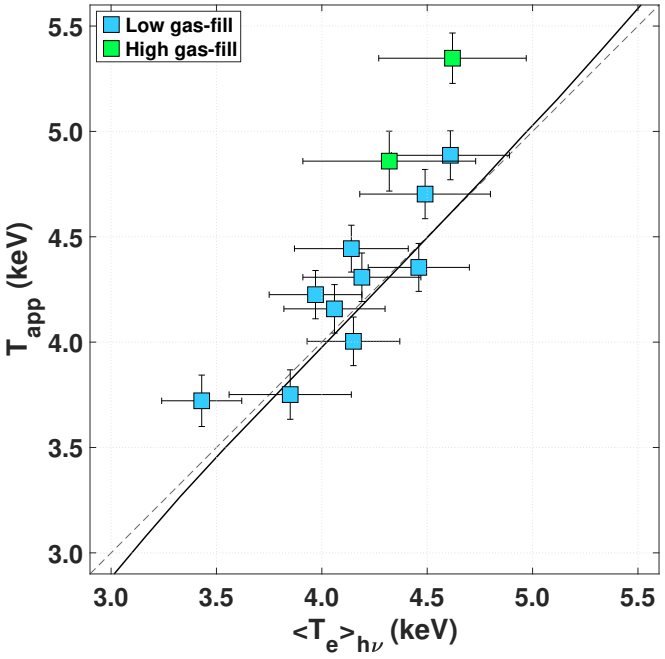

FIG. 6. Experimental measurements of the apparent ion temperature, T_{app}, measured by NTOF, and the electron temperature, $\langle T_e \rangle_{h\nu}$, measured via x-ray continuum emission. The solid line corresponds to the case of zero residual kinetic energy. Hence, the vertical offset of the data from the line represents the increase in T_{app} above the neutron-weighted thermal ion temperature due to hotspot RKE.

emission-weighted electron temperature is given by,

$$\langle T_e \rangle_{h\nu} = -\epsilon_{h\nu} \left(\frac{d\epsilon_{h\nu}}{dh\nu} \right)^{-1} \tag{10}$$

Using the 1D isobaric hotspot model we can relate the two quantities in Eqns. 8 and 10 and express one as a function of the other, $\langle T_i \rangle_n = f(\langle T_e \rangle_{h\nu})$. We find that this function is close to unity when evaluated at $h\nu = 20$ keV for temperatures in the range of $\langle T_i \rangle_n \sim$ 3–6 keV.[40] Figure 6 plots the measured T_{app} vs. $\langle T_e \rangle_{h\nu}$ from a number of recent DT experiments. The solid line represents T_{app} vs. $\langle T_e \rangle_{h\nu}$ for the case of zero residual kinetic energy, where the apparent temperature would be equal to the thermal temperature, i.e., $T_{app} = \langle T_i \rangle_n$. Hence, the vertical offset between T_{app} and the line represents additional broadening due to residual velocity flows in the hotspot. The experiments are separated by the hohlraum gas-fill density: low gas-fill ($\rho_{gas} = 0.3$ mg/cc) and high gas-fill ($\rho_{gas} = 1.6$ mg/cc). The ten low-gas fill experiments show generally good agreement between the two measurements with a mean vertical offset of $\Delta T \approx 120$ eV. The two high-gas fill experiments (both using the CH HF design) have offsets of $\Delta T \approx 540$ eV and 730 eV. These measurements are consistent with the hypothesis that the neutron-weighted thermal ion temperatures of the CH HF experiments were significantly lower than the observed NTOF apparent ion temperatures. Assuming these results to be generally applicable to all previous low and high gas-fill experiments we can apply systematic corrections to the NTOF T_{app} measurements to estimate the actual hotspot thermal ion temperatures $\langle T_i \rangle_n$.

Given experimental measurements of the neutron yield, temperature, volume, and burnwidth, we can use Eqns. 5–8 to infer the pressure P, central temperature T_o, and hotspot boundary R_o.[31] Replacing the density profile, $\rho(r)$, in Eqn. 7 by Eqn. 6 makes the radial dependence of the yield a function of just temperature. In this case T_o is given directly by the burn-weighted neutron temperature using Eqn. 8. Then, computing a normalized synthetic neutron image and matching it to the experimental image (at the 17% intensity contour) gives R_o. Finally, integrating Eqn. 7 and substituting the measure neutron yield and burnwidth gives P. Eqn. 6 then gives $\rho(r)$, with which other quantities such as the areal density can be derived. In reality, as can be seen in Fig. 5, there is no well-defined boundary between the hotspot and dense fuel. Some boundary needs to be defined, however, to infer any extrinsic property such as mass $m_{\rm hs}$, energy $E_{\rm hs}$, or areal density $\rho R_{\rm hs}$. Since our main interest is that volume that predominantly contributes to fusion yield we define an effective hotspot radius, $R_{\rm hs}$, by the central region which produces 98% of the total neutron yield.

To validate the model we use an ensemble of 2D HYDRA capsule simulations. The simulations take a nominal HDC BF design and vary a number of inputs including the capsule scale, the peak and duration of the radiation drive, $L = 1$ and $L = 2$ Legendre mode drive asymmetries, and a simple model that adds entropy to the DT fuel to mimic the effects of high-mode fuel-ablator mix.[41,42] The neutron yield, neutron-weighted ion temperature, and nuclear burnwidth are taken directly from the simulations. For the volume synthetic neutron images are generated along equatorial and polar views and the 17% intensity contours are fit with Legendre polynomial (equatorial view) or spherical harmonic (polar view) distributions, as is done with the experimental data. We compute an approximate hotspot volume bounded by the 17% intensity contour using the first two even modes, $V_{17\%} = 4\pi/3 \times (P0 + P2) \times M0^2$. The equivalent 1D radius is then $R_{17\%} = (3V_{17\%}/4\pi)^{1/3}$.

We fit the hotspot model to the synthetic data and calculate a hotspot pressure, $P_{\rm model}$, which can be compared to the neutron-weighted hotspot pressure at bangtime, $P_{\rm sim}$, extracted directly from the simulation. Figure 7 plots histograms of the ratio $P_{\rm model}/P_{\rm sim}$ showing generally good agreement across the simulation suite. For relatively symmetric implosions (hotspot $P2/P0 < 10\%$) we obtain mean and standard deviations in $P_{\rm model}/P_{\rm sim} = 1.03 \pm 0.05$. Including increasingly asymmetric implosions skews the distribution to higher values of $P_{\rm model}/P_{\rm sim}$. However, even allowing for highly distorted implosions up to hotspot $P2/P0 < 50\%$ we find the model still does a reasonably good job of inferring the true pressure with

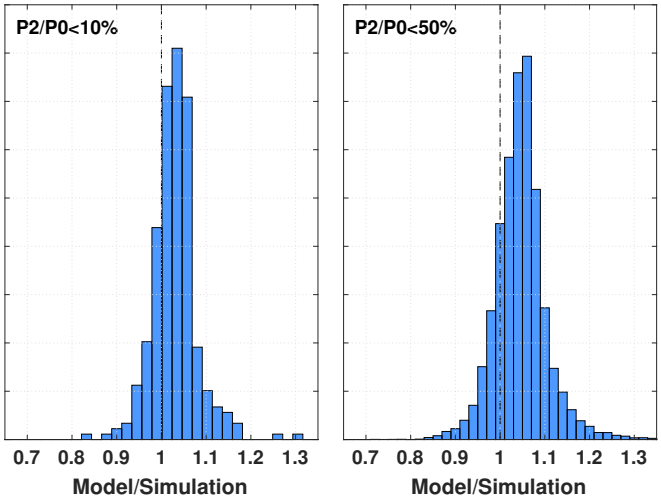

FIG. 7. Histograms of the ratio of inferred pressure from the 1D hotspot model to the neutron-weighted pressure at bangtime from the simulation for an ensemble of 2D simulated capsule implosions. The histogram on the left is restricted to relatively symmetric implosions with hotspot $P2/P0 < 10\%$ and has a mean and standard deviation of $P_{\rm model}/P_{\rm sim} = 1.03 \pm 0.05$. The histogram on the right includes highly asymmetric implosions up to $P2/P0 < 50\%$ and has a distribution of $P_{\rm model}/P_{\rm sim} = 1.05 \pm 0.10$.

$P_{\rm model}/P_{\rm sim} = 1.05 \pm 0.10$.

To apply the model to the experiments we run it over several thousand sets of measurement values obtained by Monte Carlo sampling the probability distribution of each input parameter, defined by its mean value and 1σ measurement error. We thus obtain a probability distribution for each inferred quantity, from which we can extract the mean value and standard deviation. As an example, in Table I we list the input measurements and inferred stagnation quantities for one of the highest performing HDC implosions to date (N170827). We note that for the experimental burnwidth we use the x-ray burnwidth (measured with an x-ray streak camera[43]) rather than the neutron burnwidth (measured using the gamma reaction history diagnostic[44]). The reason for this choice is the smaller uncertainty in the x-ray measurement and the fact that the measured x-ray and neutron burnwidths are statistically within ∼10 ps of each other on average.[45] Probability distributions for two of the inferred quantities, hotspot pressure and areal density, are shown in Fig. 8. The inferred stagnation pressure for this shot is $P_{\rm hs} = 337$ (-33, +42) Gbar and the hotspot areal density $\rho R_{\rm hs} = 0.311$ (-0.017, +0.019) g/cm^2. The uncertainty in $\rho R_{\rm hs}$ is relatively low because the uncertainties in $\rho_{\rm hs}$ and $R_{\rm hs}$ are correlated and partially cancel.

An important model uncertainty lies in the correct form of temperature profile $T(r)$ to use, characterized by the parameter β in Eqn. 5. We chose a value of $\beta = 0.67$ to match a HYDRA simulated profile. As seen in Fig. 5 an ideal conduction-limited profile corresponding to

TABLE I. Experimental measurements and inferred stagnation quantities for one of the highest performing HDC implosion to date (N170827). The inferred parameters $R_{\rm hs}$, $\rho R_{\rm hs}$, $m_{\rm hs}$, and $E_{\rm hs}$ are defined by the central volume producing 98% of the total neutron yield.

Parameter	Value	Uncertainty
Y_n^{DT}(neutrons)	1.89E16	±5E14
NTOF T_{app} (keV)	4.70	±0.12
Nuc $P0$ (μm)	28.4	±3.5
Nuc $P2/P0$ (%)	-27%	±5%
Nuc $M0$ (μm)	33.0	±1.2
X-ray BW (ps)	142	±13
Inferred $R_{17\%}$ (μm)	28.2	-1.9, +1.8
Inferred R_o (μm)	34.7	-2.4, +2.2
Inferred $R_{\rm hs}$ (μm)	31.8	-2.2, +2.0
Inferred $T_{\rm hs}$ (keV)	4.30	-0.26, +0.26
Inferred $\rho_{\rm hs}$ (g/cm^3)	110	-11, +13
Inferred $P_{\rm hs}$ (Gbar)	337	-33, +42
Inferred $\rho R_{\rm hs}$ (g/cm^2)	0.311	-0.017, +0.019
Inferred $m_{\rm hs}$ (μg)	16.8	-1.8, +1.8
Inferred $E_{\rm hs}$ (kJ)	6.8	-0.8, +0.7

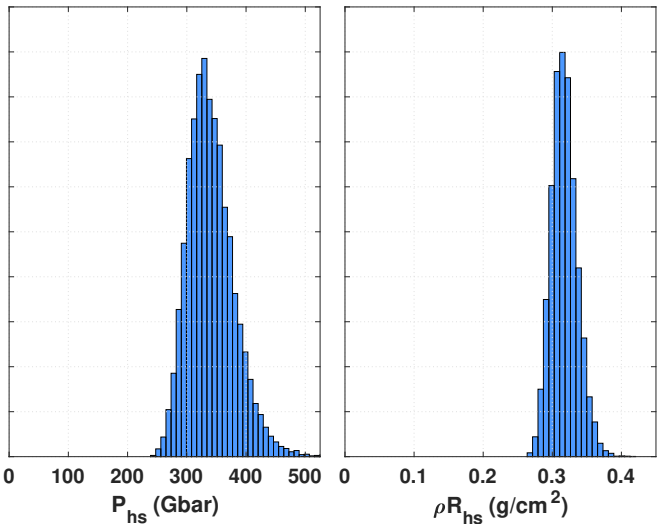

FIG. 8. Hotspot pressure and hotspot areal density probability distributions inferred for shot N170827. The mean and standard deviations are $P_{\rm hs} = 337$ (-33, +42) Gbar, and $\rho R_{\rm hs} = 0.311$ (-0.017, +0.019) g/cm^2, respectively.

β =2–2.5 would have a much steeper gradient at the hotspot boundary. On the other hand there are suggestions from detailed 3D neutron reconstructions of some shots that the profile may be more centrally peaked and less steep at the boundary.[46?] To assess the sensitivity of the inferred quantities to the precise form of temperature profile used we rerun the model for $\beta = 0$ and $\beta = 2$ and list the results in Table II. The inferred hotspot pressure and density are essentially insensitive over this range of

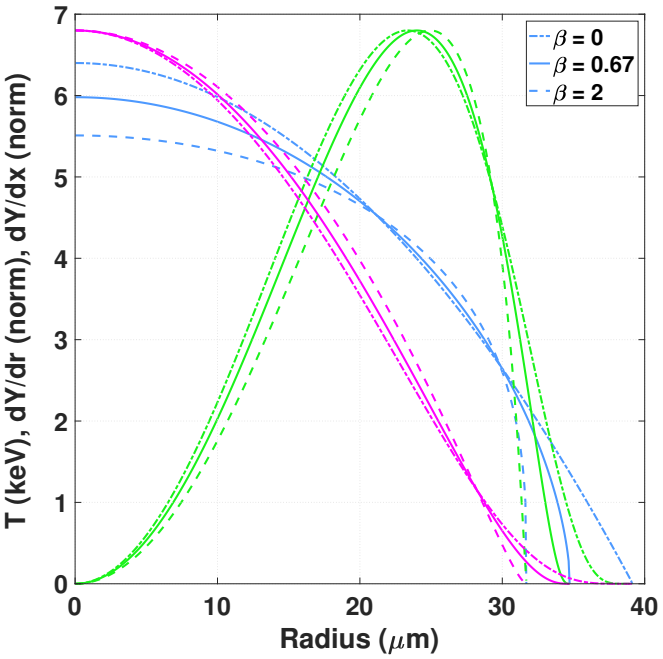

FIG. 9. Sensitivity of inferred 1D hotspot profiles to the value of β used in Eqn. 5. All profiles are constrained by the same experimental measurement inputs listed in Table I. Temperature profiles are in blue (absolute units), neutron emission per unit radius dY/dr in green (normalized to peak), and synthetic neutron image profiles dY/dx in magenta (normalized to peak).

$T(r)$ profiles, varying by no more than ±2%. The sensitivity to hotspot areal density $\rho R_{\rm hs}$ is relatively modest at ±6%. The effect on hotspot energy and mass is more significant at ±12% and ±22%, respectively. Shown in Fig. 9 are the corresponding profiles for the temperature $T(r)$, neutron emission dY_n/dr, and synthetic neutron image dY_n/dx. By construction these hotspot profiles are all constrained by the same experimentally observed yield, neutron-weighted ion temperature, 17% neutron image contour, and burnwidth. One can see that while the peak temperatures and hotspot boundaries vary the bulk of the neutron emission comes from very similar plasma conditions. The experimental observables do not well constrain either the location of, or conditions near, the hotspot boundary, resulting in larger uncertainties in those quantities strongly weighted at the large radii, such as hotspot mass and energy.

IV. HOTSPOT POWER BALANCE

We can use the inferred hotspot temperatures and areal densities to assess the net power balance in the hotspot and the proximity to ignition. We use the results of a 3D dynamic model developed by Springer *et al.*[47] In this model a 3D shell is broken up into facets where each facet is 1D and shares a common hotspot. The model

TABLE II. Dependence of inferred stagnation quantities on the value of β in the temperature profile given by Eqn. 5. The inferred values of hotspot $P_{\rm hs}$, $\rho_{\rm hs}$, and $\rho R_{\rm hs}$ are quite insensitive to the temperature profile assumed.

Parameter	$\beta = 0$	$\beta = 0.67$	$\beta = 2$
Inferred R_o (μm)	39.1	34.7	31.7
Inferred $R_{\rm hs}$ (μm)	33.3	31.8	30.3
Inferred $\rho_{\rm hs}$ (g/cm^3)	111	110	109
Inferred $P_{\rm hs}$ (Gbar)	330	337	344
Inferred $\rho R_{\rm hs}$ (g/cm^2)	0.332	0.311	0.296
Inferred $m_{\rm hs}$ (μg)	20.8	16.8	13.5
Inferred $E_{\rm hs}$ (kJ)	7.6	6.8	6.0

calculates the evolution of the hotspot pressure and temperature by evaluating the PdV work done by the faceted shell elements on the hotspot, beginning in the deceleration phase of the implosion. A key approximation is that the hotspot is isobaric and has a conduction-dominated temperature profile. In this case the thermodynamic properties of the hotspot and the rates entering the power balance can be specified as a function of time by just three parameters: the pressure P, the central temperature T, and the hotspot radius R.

The net rate of change in energy of the hotspot in an ICF implosion, Q_{net}, is given by the balance of power flow into and out of the hotspot,

$$Q_{net} = f_\alpha Q_\alpha - Q_{rad} - Q_{cond} - P\frac{dV}{dt} \qquad (11)$$

where Q_α is the alpha-particle energy production rate and f_α is the fraction of that energy deposited within the hotspot, Q_{rad} is the radiative loss rate, Q_{cond} is the conduction loss rate, and $P(dV/dt)$ is the rate of mechanical work on the hotspot, which is an energy source during the compression phase but reverses sign and is an energy sink during the explosion phase.

The net power into the hotspot is related to the hotspot temperature, T, by,

$$Q_{net} = c_P m\frac{dT}{dt} = \frac{E_{hs}}{T}\frac{dT}{dt} \qquad (12)$$

where c_P is the DT heat capacity at constant pressure, m is the hotspot mass, and E_{hs} is the hotspot energy. The hotspot temperature is then given by,

$$\frac{dT}{dt} = \frac{T}{E_{hs}}\left(f_\alpha Q_\alpha - Q_{rad} - Q_{cond} - P\frac{dV}{dt}\right) \qquad (13)$$

The hotspot volume decreases in time, reaches a minimum value on bounce, and then increases. At the time of minimum volume, $dV/dt = 0$, and we obtain the familiar Lawson condition for self-heating of a *static* hotspot,

$$\frac{dT_{\rm static}}{dt} = \frac{T}{E_{hs}}\left(f_\alpha Q_\alpha - Q_{rad} - Q_{cond}\right) > 0 \qquad (14)$$

Using analytic expressions for f_α, Q_α, Q_{rad}, and Q_{cond}, as a function of (P, R, T),[47] we can compute the Lawson self-heating boundary in the parameter space ($T_{\rm hs}$, PR), or equivalently ($T_{\rm hs}$, $\rho R_{\rm hs}$).

In Fig. 10 we plot the experimentally inferred values of ($T_{\rm hs}$, $\rho R_{\rm hs}$) for the major campaigns, as well as the static self-heating boundary. The original CH LF experiments were clearly very far from the self-heating boundary. The CH HF campaign achieved considerably better performance with hotspot temperatures reaching $T_{\rm hs} \sim 4.4$ keV and hotspot areal densities $\rho R_{\rm hs} \sim 0.2$ g/cm^2. Lastly, in the HDC and HDC BF campaigns implosions reached similar temperatures to CH HF, but up to 50% higher areal densities, reaching $\rho R_{\rm hs} \sim 0.3$ g/cm^2. This is likely due to improved symmetry and shell confinement, which allows more time for the hotspot to accumulate mass through ablation of the inner surface of the DT shell, thereby increasing both hotspot mass and areal density.

The self-heating boundary shown in Fig. 10 applies to a clean DT hotspot. However, experiments have often shown signatures of high-Z ablator mix entering the hotspot, typically from perturbations seeded by engineering features such as the fill-tube, support tent, or particulates on the capsule surface.[5,49,50] High-Z mix increases the radiation loss from the hotspot and can be accounted for in the radiative loss term as $Q_{rad} = Q_{DT} + Q_{mix}$. The effect is to increase the temperature required to meet the self-heating condition. As an example the change in the self-heating boundary for the case of a 20% increase in radiative loss due to mix ($Q_{mix}/Q_{DT} = 20\%$) is shown in Fig. 11. Excess radiative loss from ablator mix seeded by the fill-tube alone has been estimated from x-ray imaging data to vary between 2-14% across a subset of shots analysed.[46?] Mix observed from other seeds, such as surface particulates, which vary shot to shot, can significantly add to the total radiative loss.

The self-heating condition, $dT/dt > 0$, is a necessary but insufficient condition for ignition. On expansion of the hotspot, PdV work is a loss term, and for the hotspot to ignite it is necessary that at the time of minimum volume the net alpha-heating heating rate is both positive and also increasing faster than the rate of PdV expansion. This is equivalent to requiring both the first and second derivatives of temperature to be greater than zero at minimum volume. As described in[47] the second derivative condition, $d^2T/dt^2 > 0$, can be estimated by expanding Eqn. 13 about the minimum volume to obtain

$$\begin{aligned} \frac{d^2 T_{\rm static}}{dt^2} &> \frac{2}{3}\frac{T}{V}\frac{d^2 V}{dt^2} \\ &> \frac{2}{3}\frac{T}{V}\int r^2\ddot{r} + 2r\dot{r}^2\, d\Omega \end{aligned} \tag{15}$$

The right hand side contains two terms. The first term includes the radial acceleration of the hotspot boundary, $\ddot{r}$, and can be regarded as a confinement parameter. The acceleration is approximately the differential pressure across the stagnated shell over the areal density of the shell, $\ddot{r} \approx \Delta P/\rho R_{\rm shell}$. The second term includes the radial velocity, $\dot{r}$, and represents residual shell velocity which would be non-zero in the presence of 3D shape asymmetry. In the limit of a 1D implosion with an infinitely thick shell the right hand side of Eqn. 15 is zero and the second derivative ignition condition is automatically met by the static self-heating condition, $dT/dt > 0$. However, as the shell areal density decreases the second derivative boundary moves up in temperature and the ignition parameter space becomes increasingly more restricted. Figure 11 shows the $d^2T/dt^2 > 0$ region for the example case of $\rho R_{\rm shell} = 1$ g/cm^2. We see that for hotspot areal densities of $\rho R_{hs} \sim 0.3$ g/cm^2 the temperature required for ignition increases from 4.8 keV in the static case to 5.7 keV in the dynamic case.

In Fig. 12 we plot a simulated trajectory through $T_{\rm hs}$–$\rho R_{\rm hs}$ space from a nominal 2D capsule simulation that reproduces the neutron yield (∼52 kJ) of one of the highest performing HDC implosions. In the simulation the hotspot temperature rises quickly to ∼4.8 keV and then remains relatively flat while the effects of convergence and mass ablation of DT ice increase the hotspot $\rho R_{\rm hs}$. The black circle shows the neutron-weighted $T_{\rm hs}$ and $\rho R_{\rm hs}$ integrated over time. The white circle is the value of $T_{\rm hs}$ and $\rho R_{\rm hs}$ at the time of minimum volume in the simulation. The black circle is more representative of the inferred values from the experimental data. We do not directly measure the minimum volume conditions given by the white circle, which are the ones relevant for comparing to the self-heating and ignition curves. Though at these implosion conditions the time-integrated and minimum volume time $T_{\rm hs}$–$\rho R_{\rm hs}$ values are fairly similar because the minimum volume time is very close—within 20 ps—of the peak neutron production time. We see that at minimum volume the hotspot has just crossed the $dT/dt > 0$ boundary but failed to cross the $d^2T/dt^2 > 0$ boundary resulting in a non-igniting implosion.

To illustrate how the behavior of the hotspot changes as we approach ignition we performed additional capsule simulations, shown in Fig. 13, at progressively larger hydrodynamic scales, ranging from 1.1x to 1.35x of the baseline case. At 1.1x scale the temperature is increasing at minimum volume but still $d^2T/dt^2 < 0$ and the implosion fails to ignite. At 1.25x scale the minimum volume point is right on the $d^2T/dt^2 = 0$ boundary and the hotspot is just at the point of igniting, with the yield boosted to 380 kJ. Finally, at 1.35x scale the minimum volume point has crossed well into the $d^2T/dt^2 > 0$ region and the implosion ignites with 2.5 MJ yield. The behavior of the simulations is therefore consistent with the model-based ignition criterion. However, we should note that the $d^2T/dt^2 = 0$ boundary shown in these plots is representative of a specific implosion configuration and in actuality it will differ for each individual simulation or experiment depending on the particular values of mix, shell areal density, and 3D asymmetry.

We can further verify the relationship between the temperature derivative and the ignition boundary by directly

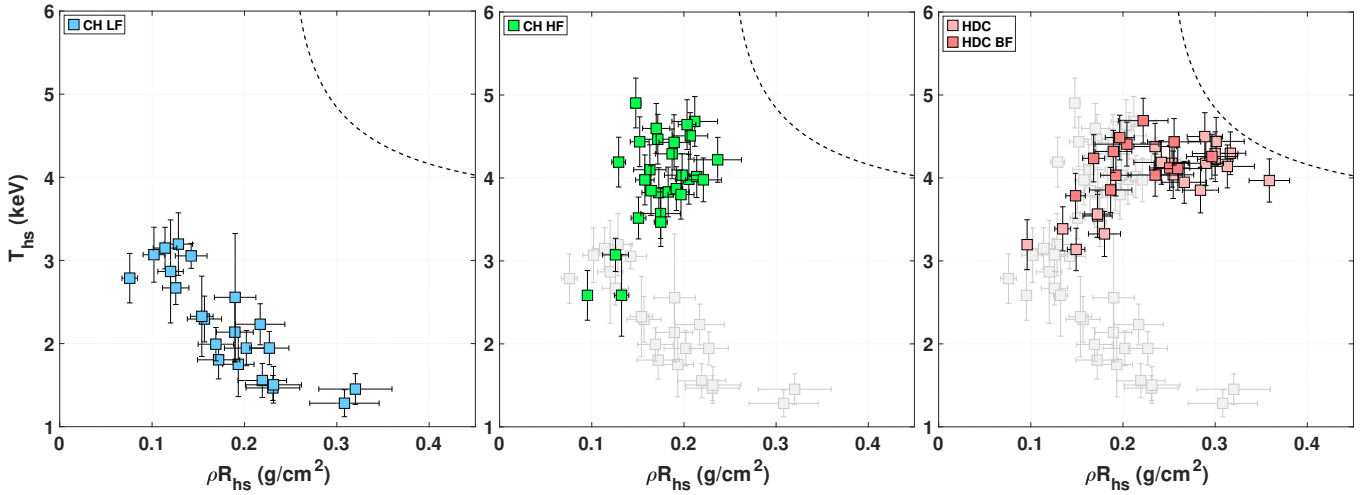

FIG. 10. Hotspot temperature, $T_{\rm hs}$, and areal density, $\rho R_{\rm hs}$, of DT implosion experiments in the CH LF (left), CH HF (middle), and HDC and HDC BF campaigns (right). The dashed line is the Lawson self-heating boundary ($dT/dt = 0$), for a static plasma ($dV/dt = 0$). These are similar to the plots shown in Hurricane *et al.*[48] but use updated values for the inferred stagnation quantities using the static hotspot model described above.

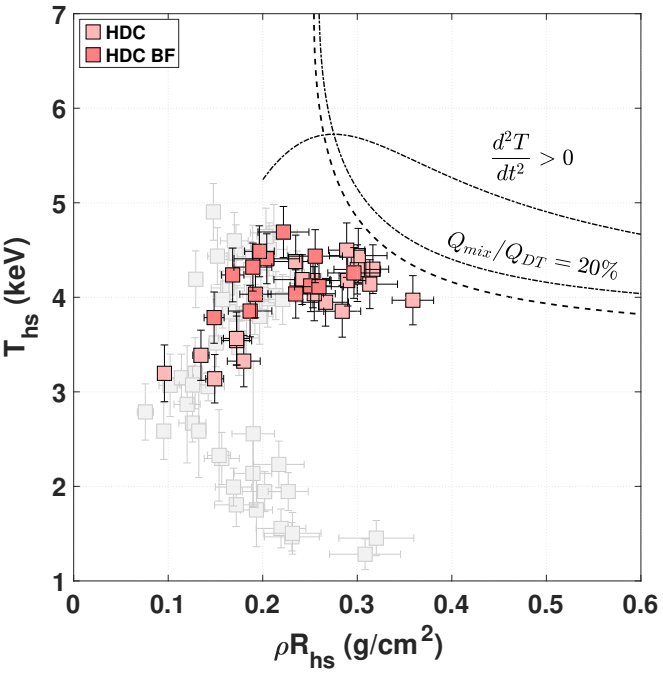

FIG. 11. Effect of mix and expansion work on moving the self-heating and ignition boundaries. The dashed line is the Lawson self-heating boundary ($dT/dt = 0$) for a clean static DT hotspot. The lower dot-dash line is the boundary for a case where mix in the hotspot increases the radiative loss by 20%, i.e., $Q_{mix}/Q_{DT} = 20\%$. The upper dot-dash line is the ignition requirement, $d^2T/dt^2 = 0$, for a $\rho R_{\rm shell} = 1$ g/cm^2 (this line is for a clean DT or $Q_{mix} = 0$ case).

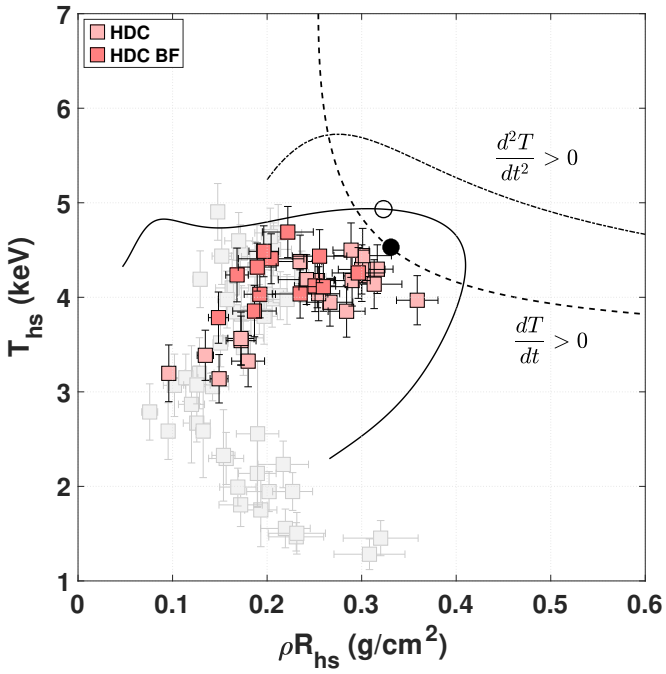

FIG. 12. Simulated trajectory through $T_{\rm hs}$–$\rho R_{\rm hs}$ space from a nominal 2D simulation of an HDC implosion. The black circle is the time-integrated neutron-weighted temperature and hotspot areal density. The white circle is the neutron-weighted temperature and hotspot areal density at the minimum volume time of the implosion.

examining the time-derivative of the hotspot temperature in the simulations. In Fig. 14 we plot the hotspot temperature as a function of time for the same four simulations with the horizontal axis being the time relative to the time of minimum volume for each simulation. We see that for the first two implosions (producing 52 and 100 kJ) the second derivatives of temperature are less than zero at the time of minimum volume (i.e, the slopes of the lines, or first derivatives, are decreasing). In the third im-

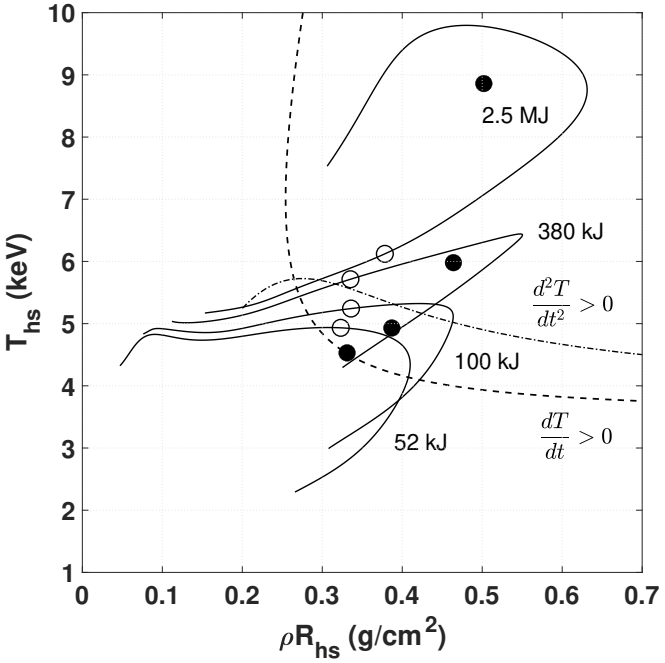

FIG. 13. Simulated trajectories from a set of 2D capsule simulations varying in scale from a nominal 1x to 1.1x, 1.25x, and 1.35x. The total neutron yield is shown for each simulation. Black circles are the time-integrated neutron-weighted temperature and hotspot areal density. White circles are the neutron-weighted temperature and hotspot areal density at the minimum volume time of the implosion.

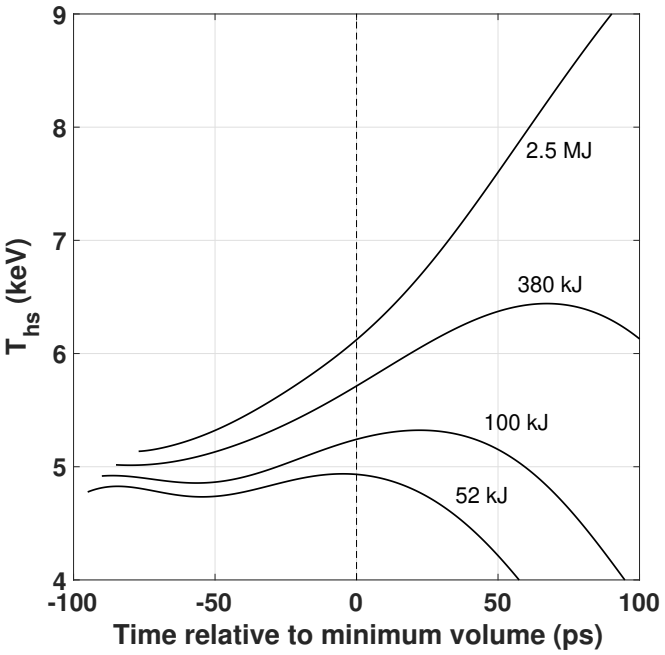

FIG. 14. Simulated hotspot temperature as a function of time for the four implosions shown in Fig. 13. The horizontal axis is the time relative to the time of minimum volume for each implosion. The curves are labeled by their total neutron yields.

plosion the second derivative is close to zero. And in the fourth implosion—which robustly ignites—it is greater than zero. Another interesting observation from this plot is that the difference in time between minimum volume and peak neutron production (which is close to peak pressure, and approximately peak temperature) increases as we approach ignition. Thus, it is the power balance in the hotspot at a time *prior* to peak neutron production and pressure that determine whether or not the hotspot will ignite.

V. CONCLUSIONS

We have described the overall performance of ICF implosions on the NIF and their proximity to ignition both in terms of the no-burn ignition parameter, $\chi_{n\alpha}$, which depends on the yield and the total fuel areal density, and in terms of the inferred hotspot stagnation conditions. The best performing implosions to date have achieved values of $\chi_{n\alpha} \approx 0.75$, corresponding to yield amplifications from alpha-heating of $2.55\text{x} \pm 0.17$. As can be seen in Figs. 3 and 4 relatively small improvements in the no-burn $\chi_{n\alpha}$ metric from current experiments would be expected to produce significant increases in both yield amplification and total fusion yield. In terms of hotspot stagnation conditions a number of HDC ablator implosions are estimated to have reached neutron-weighted thermal ion temperatures of $T_{\rm hs} \sim 4.4$ keV and hotspot areal densities of $\rho R_{\rm hs} \sim 0.3$ g/cm^2. These conditions are very close to the self-heating boundary, $dT/dt > 0$, at minimum volume. The ignition boundary, $d^2T/dt^2 > 0$, is somewhat further away, with its precise location being strongly dependent on the shell areal density and 3D shell asymmetry that determine the confinement parameter, and to the degree of hotspot mix which increases the radiation loss term. The gap between current experiments and the ignition boundary can be closed by both further improving the hotspot conditions in terms of pressure, temperature, and areal density to move well into the self-heating regime, and from the other direction by bringing the $d^2T/dt^2 = 0$ ignition boundary closer by increasing the shell areal density, reducing 3D shell asymmetry, and reducing hotspot mix.

We note that since the ignition criteria are described here in terms of the hotspot conditions at minimum volume it would be valuable to measure the time-dependent hotspot temperature and areal density. Currently, we have time-resolved measurements of the neutron production rate and the hotspot size (through time-resolved x-ray imaging). A cross-timed time-resolved temperature measurement would enable a determination of the $T_{\rm hs}$–$\rho R_{\rm hs}$ conditions at the minimum volume time. Two new diagnostics are under development that could provide this information: first, a time-resolved magnetic recoil spectrometer (MRS-t) measuring time-resolved T_i,[51] and second, a time-resolved x-ray continuum measurement to infer the time-resolved T_e.[52]

ACKNOWLEDGMENTS

This work was performed under the auspices of the U.S. Department of Energy by Lawrence Livermore National Laboratory under Contract DE-AC52-07NA27344. This document was prepared as an account of work sponsored by an agency of the United States government. Neither the United States government nor Lawrence Livermore National Security, LLC, nor any of their employees makes any warranty, expressed or implied, or assumes any legal liability or responsibility for the accuracy, completeness, or usefulness of any information, apparatus, product, or process disclosed, or represents that its use would not infringe privately owned rights. Reference herein to any specific commercial product, process, or service by trade name, trademark, manufacturer, or otherwise does not necessarily constitute or imply its endorsement, recommendation, or favoring by the United States government or Lawrence Livermore National Security, LLC. The views and opinions of authors expressed herein do not necessarily state or reflect those of the United States government or Lawrence Livermore National Security, LLC, and shall not be used for advertising or product endorsement purposes.

[1] J. Nuckolls and L. Wood, Nature **239**, 139 (1972).
[2] J. D. Lindl, P. Amendt, R. L. Berger, S. G. Glendinning, S. H. Glenzer, S. W. Haan, R. L. Kauffman, O. L. Landen, and L. J. Suter, Physics of Plasmas **11**, 339 (2004).
[3] J. A. Frenje, R. Bionta, E. J. Bond, J. A. Caggiano, D. T. Casey, C. Cerjan, J. Edwards, M. Eckart, D. N. Fittinghoff, S. Friedrich, V. Y. Glebov, S. Glenzer, G. Grim, S. Haan, R. Hatarik, S. Hatchett, M. G. Johnson, O. S. Jones, J. D. Kilkenny, J. P. Knauer, O. Landen, R. Leeper, S. L. Pape, R. Lerche, C. K. Li, A. Mackinnon, J. McNaney, F. E. Merrill, M. Moran, D. H. Munro, T. J. Murphy, R. D. Petrasso, R. Rygg, T. C. Sangster, F. H. Séguin, S. Sepke, B. Spears, P. Springer, C. Stoeckl, and D. C. Wilson, Nuclear Fusion **53**, 043014 (2013).
[4] D. S. Clark, M. M. Marinak, C. R. Weber, D. C. Eder, S. W. Haan, B. A. Hammel, D. E. Hinkel, O. S. Jones, J. L. Milovich, P. K. Patel, H. F. Robey, J. D. Salmonson, S. M. Sepke, and C. A. Thomas, Physics of Plasmas **22**, 022703 (2015).
[5] T. Ma, P. K. Patel, N. Izumi, P. T. Springer, M. H. Key, L. J. Atherton, L. R. Benedetti, D. K. Bradley, D. A. Callahan, P. M. Celliers, C. J. Cerjan, D. S. Clark, E. L. Dewald, S. N. Dixit, T. Doppner, D. H. Edgell, R. Epstein, S. Glenn, G. Grim, S. W. Haan, B. A. Hammel, D. Hicks, W. W. Hsing, O. S. Jones, S. F. Khan, J. D. Kilkenny, J. L. Kline, G. A. Kyrala, O. L. Landen, S. Le Pape, B. J. MacGowan, A. J. Mackinnon, A. G. MacPhee, N. B. Meezan, J. D. Moody, A. Pak, T. Parham, H. S. Park, J. E. Ralph, S. P. Regan, B. A. Remington, H. F. Robey, J. S. Ross, B. K. Spears, V. Smalyuk, L. J. Suter, R. Tommasini, R. P. Town, S. V. Weber, J. D. Lindl, M. J. Edwards, S. H. Glenzer, and E. I. Moses, Physical Review Letters **111**, 085004 (2013).
[6] O. A. Hurricane, D. A. Callahan, D. T. Casey, E. L. Dewald, T. R. Dittrich, T. Doppner, M. A. Barrios Garcia, D. E. Hinkel, L. F. Berzak Hopkins, P. Kervin, J. L. Kline, S. L. Pape, T. Ma, A. G. MacPhee, J. L. Milovich, J. Moody, A. Pak, P. K. Patel, H. S. Park, B. A. Remington, H. F. Robey, J. D. Salmonson, P. T. Springer, R. Tommasini, L. R. Benedetti, J. A. Caggiano, P. Celliers, C. Cerjan, R. Dylla-Spears, D. Edgell, M. J. Edwards, D. Fittinghoff, G. P. Grim, N. Guler, N. Izumi, J. A. Frenje, M. Gatu Johnson, S. Haan, R. Hatarik, H. Herrmann, S. Khan, J. Knauer, B. J. Kozioziemski, A. L. Kritcher, G. Kyrala, S. A. Maclaren, F. E. Merrill, P. Michel, J. Ralph, J. S. Ross, J. R. Rygg, M. B. Schneider, B. K. Spears, K. Widmann, and C. B. Yeamans, Physics of Plasmas **21**, 056314 (2014).
[7] O. A. Hurricane, D. A. Callahan, D. T. Casey, P. M. Celliers, C. Cerjan, E. L. Dewald, T. R. Dittrich, T. Doppner, D. E. Hinkel, L. F. B. Hopkins, J. L. Kline, S. Le Pape, T. Ma, A. G. MacPhee, J. L. Milovich, A. Pak, H. S. Park, P. K. Patel, B. A. Remington, J. D. Salmonson, P. T. Springer, and R. Tommasini, Nature , 1 (2014).
[8] D. S. Clark, J. L. Milovich, D. E. Hinkel, J. D. Salmonson, J. L. Peterson, L. F. B. Hopkins, D. C. Eder, S. W. Haan, O. S. Jones, M. M. Marinak, H. F. Robey, V. A. Smalyuk, and C. R. Weber, Physics of Plasmas **21**, 112705 (2014).
[9] A. G. MacPhee, J. L. Peterson, D. T. Casey, D. S. Clark, S. W. Haan, O. S. Jones, O. L. Landen, J. L. Milovich, H. F. Robey, and V. A. Smalyuk, Physics of Plasmas **22**, 080702 (2015).
[10] V. A. Smalyuk, H. F. Robey, T. Doppner, D. T. Casey, D. S. Clark, O. S. Jones, J. L. Milovich, J. L. Peterson, B. Bachmann, K. L. Baker, L. R. Benedetti, L. F. B. Hopkins, R. Bionta, E. Bond, D. K. Bradley, D. A. Callahan, P. M. Celliers, C. Cerjan, K. C. Chen, C. Goyon, G. Grim, S. N. Dixit, M. J. Eckart, M. J. Edwards, M. Farrell, D. N. Fittinghoff, J. A. Frenje, M. Gatu Johnson, N. Gharibyan, S. W. Haan, A. V. Hamza, E. Hartouni, R. Hatarik, M. Havre, M. Hohenberger, D. Hoover, O. A. Hurricane, N. Izumi, K. S. Jancaitis, S. F. Khan, J. P. Knauer, J. J. Kroll, G. Kyrala, K. N. LaFortune, O. L. Landen, T. Ma, B. J. MacGowan, A. G. MacPhee, M. Mauldin, F. E. Merrill, A. S. Moore, S. Nagel, A. Nikroo, A. Pak, P. K. Patel, J. E. Ralph, D. B. Sayre, D. Shaughnessy, B. K. Spears, R. Tommasini, D. P. Turnbull, A. L. Velikovich, P. L. Volegov, C. R. Weber, C. C. Widmayer, and C. Yeamans, Physics of Plasmas **23**, 102703 (2016).
[11] J. D. Moody, D. A. Callahan, D. E. Hinkel, P. A. Amendt, K. L. Baker, D. Bradley, P. M. Celliers, E. L. Dewald, L. Divol, T. Doeppner, D. C. Eder, M. J. Edwards, O. Jones, S. W. Haan, D. Ho, L. B. Hopkins, N. Izumi, D. Kalantar, R. L. Kauffman, J. D. Kilkenny, O. Landen, B. Lasinski, S. LePape, T. Ma, B. J. MacGowan, S. A. Maclaren, A. J. Mackinnon, D. Meeker, N. Meezan, P. Michel, J. L. Milovich, D. Munro, A. Pak, M. Rosen, J. Ralph, H. F. Robey, J. S. Ross, M. B. Schneider, D. Strozzi, E. Storm, C. Thomas, R. P. J. Town, K. L. Widmann, J. Kline, G. Kyrala, A. Nikroo, T. Boehly, A. S. Moore, and S. H. Glenzer, Physics of Plasmas **21** (2014).
[12] A. L. Kritcher, D. E. Hinkel, D. A. Callahan, O. A. Hurricane, D. Clark, D. T. Casey, E. L. Dewald, T. R. Dittrich, T. Doppner, M. A. Barrios Garcia, S. Haan, L. F. Berzak Hopkins, O. Jones, O. Landen, T. Ma, N. Meezan, J. L. Milovich, A. Pak, H. S. Park, P. K. Patel, J. Ralph, H. F. Robey, J. D. Salmonson, S. Sepke, B. Spears, P. T. Springer, C. A. Thomas, R. Town, P. M. Celliers, and M. J. Edwards, Physics of Plasmas **23**, 052709 (2016).
[13] L. F. Berzak Hopkins, N. B. Meezan, S. Le Pape, L. Divol, A. J. Mackinnon, D. D. Ho, M. Hohenberger, O. S. Jones, G. Kyrala, J. L. Milovich, A. Pak, J. E. Ralph, J. S. Ross, L. R. Benedetti, J. Biener, R. Bionta, E. Bond, D. Bradley, J. Caggiano, D. Callahan, C. Cerjan, J. Church, D. Clark, T. Doppner, R. Dylla-Spears, M. Eckart, D. Edgell, J. Field, D. N. Fittinghoff, M. Gatu Johnson, G. Grim, N. Guler, S. Haan, A. Hamza, E. P. Hartouni, R. Hatarik, H. W. Herrmann, D. Hinkel, D. Hoover, H. Huang, N. Izumi, S. Khan, B. Kozioziemski, J. Kroll, T. Ma, A. MacPhee, J. McNaney, F. Merrill, J. Moody, A. Nikroo, P. Patel, H. F. Robey, J. R. Rygg, J. Sater, D. Sayre, M. Schneider, S. Sepke, M. Stadermann, W. Stoeffl, C. Thomas, R. P. J. Town, P. L. Volegov, C. Wild, C. Wilde, E. Woerner, C. Yeamans, B. Yoxall, J. Kilkenny, O. L. Landen, W. Hsing, and M. J. Edwards, Physical Review Letters **114**, 175001 (2015).
[14] S. Le Pape, L. F. Berzak Hopkins, L. Divol, A. Pak, E. L. Dewald, S. Bhandarkar, L. R. Bennedetti, T. Bunn, J. Biener, J. Crippen, D. Casey, D. Edgell, D. N. Fittinghoff, M. Gatu Johnson, C. Goyon, S. Haan, R. Hatarik, M. Havre, D. D.-M. Ho, N. Izumi, J. Jaquez, S. F. Khan, G. A. Kyrala, T. Ma, A. J. Mackinnon, A. G. MacPhee, B. J. MacGowan, N. B. Meezan, J. Milovich,

M. Millot, P. Michel, S. R. Nagel, A. Nikroo, P. Patel, J. Ralph, J. S. Ross, N. G. Rice, D. Strozzi, M. Stadermann, P. Volegov, C. Yeamans, C. Weber, C. Wild, D. Callahan, and O. A. Hurricane, Physical Review Letters **120**, 245003 (2018).
[15]L. B. Hopkins, S. LePape, L. Divol, A. Pak, E. Dewald, D. D. Ho, N. Meezan, S. Bhandarkar, L. R. Benedetti, T. Bunn, J. Biener, J. Crippen, D. Casey, D. Clark, D. Edgell, D. Fittinghoff, M. Gatu Johnson, C. Goyon, S. Haan, R. Hatarik, M. Havre, D. Hinkel, H. Huang, N. Izumi, J. Jaquez, O. Jones, S. Khan, A. Kritcher, C. Kong, G. Kyrala, O. Landen, T. Ma, A. MacPhee, B. MacGowan, A. J. Mackinnon, M. Marinak, J. Milovich, M. Millot, P. Michel, A. Moore, S. R. Nagel, A. Nikroo, P. Patel, J. Ralph, H. Robey, J. S. Ross, N. G. Rice, S. Sepke, V. A. Smalyuk, P. Sterne, D. Strozzi, M. Stadermann, P. Volegov, C. Weber, C. Wild, C. Yeamans, D. Callahan, O. Hurricane, R. P. J. Town, and M. J. Edwards, Plasma Physics and Controlled Fusion **61**, 014023 (2018).
[16]C. Thomas, Bulletin of the American Physical Society **64** (2019).
[17]K. L. Baker, C. A. Thomas, D. T. Casey, S. Khan, B. K. Spears, R. Nora, T. Woods, J. L. Milovich, R. L. Berger, D. Strozzi, D. Clark, M. Hohenberger, O. A. Hurricane, D. A. Callahan, O. L. Landen, B. Bachmann, R. Benedetti, R. Bionta, P. M. Celliers, D. Fittinghoff, C. Goyon, G. Grim, R. Hatarik, N. Izumi, M. G. Johnson, G. Kyrala, T. Ma, M. Millot, S. R. Nagel, A. Pak, P. K. Patel, D. Turnbull, P. L. Volegov, and C. Yeamans, Physical Review Letters **121** (2018).
[18]A. L. Kritcher, (in preparation).
[19]M. Hohenberger, (in preparation).
[20]B. K. Spears, S. Glenzer, M. J. Edwards, S. Brandon, D. Clark, R. Town, C. Cerjan, R. Dylla-Spears, E. Mapoles, D. Munro, J. Salmonson, S. Sepke, S. Weber, S. Hatchett, S. Haan, P. Springer, E. Moses, J. Kline, G. Kyrala, and D. Wilson, Physics of Plasmas **19**, 056316 (2012).
[21]J. Lindl, O. Landen, J. Edwards, E. Moses, and NIC Team, Physics of Plasmas **21**, 020501 (2014).
[22]J. D. Lindl, S. W. Haan, O. L. Landen, A. R. Christopherson, and R. Betti, Physics of Plasmas **25**, 122704 (2018).
[23]S. W. Haan, J. D. Lindl, D. A. Callahan, D. S. Clark, J. D. Salmonson, B. A. Hammel, L. J. Atherton, R. C. Cook, M. J. Edwards, S. Glenzer, A. V. Hamza, S. P. Hatchett, M. C. Herrmann, D. E. Hinkel, D. D. Ho, H. Huang, O. S. Jones, J. Kline, G. Kyrala, O. L. Landen, B. J. MacGowan, M. M. Marinak, D. D. Meyerhofer, J. L. Milovich, K. A. Moreno, E. I. Moses, D. H. Munro, A. Nikroo, R. E. Olson, K. Peterson, S. M. Pollaine, J. E. Ralph, H. F. Robey, B. K. Spears, P. T. Springer, L. J. Suter, C. A. Thomas, R. P. Town, R. Vesey, S. V. Weber, H. L. Wilkens, and D. C. Wilson, Physics of Plasmas **18**, 051001 (2011).
[24]D. S. Clark, D. E. Hinkel, D. C. Eder, O. S. Jones, S. W. Haan, B. A. Hammel, M. M. Marinak, J. L. Milovich, H. F. Robey, L. J. Suter, and R. P. J. Town, Physics of Plasmas **20**, 056318 (2013).
[25]A. R. Christopherson, R. Betti, and J. D. Lindl, Physical Review E **99**, 021201 (2019).
[26]R. Betti, A. R. Christopherson, B. K. Spears, R. Nora, A. Bose, J. Howard, K. M. Woo, M. J. Edwards, and J. Sanz, Physical Review Letters **114**, 255003 (2015).
[27]C. D. Zhou and R. Betti, Physics of Plasmas **15**, 102707 (2008).
[28]P. Y. Chang, R. Betti, B. K. Spears, K. S. Anderson, J. Edwards, M. Fatenejad, J. D. Lindl, R. L. McCrory, R. Nora, and D. Shvarts, Physical Review Letters **104**, 135002 (2010).
[29]R. Nora, R. Betti, K. S. Anderson, A. Shvydky, A. Bose, K. M. Woo, A. R. Christopherson, J. A. Marozas, T. J. B. Collins, P. B. Radha, S. X. Hu, R. Epstein, F. J. Marshall, R. L. McCrory, T. C. Sangster, and D. D. Meyerhofer, Physics of Plasmas **21** (2014).
[30]P. T. Springer, C. Cerjan, R. Betti, J. A. Caggiano, M. J. Edwards, J. A. Frenje, V. Y. Glebov, S. H. Glenzer, S. M. Glenn, N. Izumi, O. Jones, G. Kyrala, T. Ma, J. McNaney, M. Moran, D. H. Munro, S. Regan, T. C. Sangster, S. Sepke, H. Scott, R. P. J. Town, S. V. Weber, and B. Wilson, EPJ Web of Conferences **59**, 04001 (2013).
[31]C. Cerjan, P. T. Springer, and S. M. Sepke, Physics of Plasmas **20**, 056319 (2013).
[32]R. Betti, M. Umansky, V. Lobatchev, V. N. Goncharov, and R. L. McCrory, Physics of Plasmas **8**, 5257 (2001).
[33]H. Brysk, Plasma Physics **15**, 611 (1973).
[34]V. Y. Glebov, T. C. Sangster, C. Stoeckl, J. P. Knauer, W. Theobald, K. L. Marshall, M. J. Shoup, T. Buczek, M. Cruz, T. Duffy, M. Romanofsky, M. Fox, A. Pruyne, M. J. Moran, R. A. Lerche, J. McNaney, J. D. Kilkenny, M. J. Eckart, D. Schneider, D. Munro, W. Stoeffl, R. Zacharias, J. J. Haslam, T. Clancy, M. Yeoman, D. Warwas, C. J. Horsfield, J. L. Bourgade, O. Landoas, L. Disdier, G. A. Chandler, and R. J. Leeper, Review of Scientific Instruments **81**, 10D325 (2010).
[35]T. J. Murphy, Physics of Plasmas **21**, 072701 (2014).
[36]D. H. Munro, Nuclear Fusion **56**, 036001 (2016).
[37]D. S. Clark, C. R. Weber, J. L. Milovich, J. D. Salmonson, A. L. Kritcher, S. W. Haan, B. A. Hammel, D. E. Hinkel, O. A. Hurricane, O. S. Jones, M. M. Marinak, P. K. Patel, H. F. Robey, S. M. Sepke, and M. J. Edwards, Physics of Plasmas **23**, 056302 (2016).
[38]O. A. Hurricane, D. A. Callahan, D. T. Casey, E. L. Dewald, T. R. Dittrich, T. Doppner, S. Haan, D. E. Hinkel, L. F. Berzak Hopkins, O. Jones, A. L. Kritcher, S. Le Pape, T. Ma, A. G. MacPhee, J. L. Milovich, J. Moody, A. Pak, H. S. Park, P. K. Patel, J. E. Ralph, H. F. Robey, J. S. Ross, J. D. Salmonson, B. K. Spears, P. T. Springer, R. Tommasini, F. Albert, L. R. Benedetti, R. Bionta, E. Bond, D. K. Bradley, J. Caggiano, P. M. Celliers, C. Cerjan, J. A. Church, R. Dylla-Spears, D. Edgell, M. J. Edwards, D. Fittinghoff, M. A. Barrios Garcia, A. Hamza, R. Hatarik, H. Herrmann, M. Hohenberger, D. Hoover, J. L. Kline, G. Kyrala, B. Kozioziemski, G. Grim, J. E. Field, J. Frenje, N. Izumi, M. Gatu Johnson, S. F. Khan, J. Knauer, T. Kohut, O. Landen, F. Merrill, P. Michel, A. Moore, S. R. Nagel, A. Nikroo, T. Parham, R. R. Rygg, D. Sayre, M. Schneider, D. Shaughnessy, D. Strozzi, R. P. J. Town, D. Turnbull, P. Volegov, A. Wan, K. Widmann, C. Wilde, and C. Yeamans, Nature Physics , 1 (2016).
[39]L. C. Jarrott, L. R. Benedetti, H. Chen, N. Izumi, S. F. Khan, T. Ma, S. R. Nagel, O. L. Landen, A. Pak, P. K. Patel, M. Schneider, and H. A. Scott, Review of Scientific Instruments **87**, 11E534 (2016).
[40]L. C. Jarrott, B. Bachmann, T. Ma, L. R. Benedetti, F. E. Field, E. P. Hartouni, R. Hatarik, N. Izumi, S. F. Khan, O. L. Landen, S. R. Nagel, R. Nora, A. Pak, J. L. Peterson, M. B. Schneider, P. T. Springer, and P. K. Patel, Physical Review Letters **121**, 085001 (2018).
[41]R. Nora, J. L. Peterson, B. K. Spears, J. E. Field, and S. Brandon, Statistical Analysis and Data Mining: The ASA Data Science Journal **10**, 230 (2017).
[42]J. A. Gaffney, S. T. Brandon, K. D. Humbird, M. K. G. Kruse, R. C. Nora, J. L. Peterson, and B. K. Spears, Physics of Plasmas , 1 (2019).
[43]S. F. Khan, P. M. Bell, D. K. Bradley, S. R. Burns, J. R. Celeste, L. S. Dauffy, M. J. Eckart, M. A. Gerhard, C. Hagmann, D. I. Headley, J. P. Holder, N. Izumi, M. C. Jones, J. W. Kellogg, H. Y. Khater, J. R. Kimbrough, A. G. MacPhee, Y. P. Opachich, N. E. Palmer, R. B. Petre, J. L. Porter, R. T. Shelton, T. L. Thomas, and J. B. Worden, in *SPIE Optical Engineering + Applications*, edited by P. Bell and G. P. Grim (SPIE, 2012) pp. 850505–9.
[44]H. W. Herrmann, N. Hoffman, D. C. Wilson, W. Stoeffl, L. Dauffy, Y. H. Kim, A. McEvoy, C. S. Young, J. M. Mack, C. J. Horsfield, M. Rubery, E. K. Miller, and Z. A. Ali, Review of Scientific Instruments **81**, 10D333 (2010).
[45]G. Williams, Bulletin of the American Physical Society, http://meetings.aps.org/link/BAPS.2018.DPP.PO6.2 (2018).
[46]L. Divol, Bulletin of the American Physical Society **64** (2019).
[47]P. T. Springer, O. A. Hurricane, J. H. Hammer, R. Betti, D. A. Callahan, E. M. Campbell, D. T. Casey, C. J. Cerjan, D. Cao, E. Dewald, L. Divol, T. Doeppner, M. J. Edwards, J. E. Field, C. Forrest, J. Frenje, J. A. Gaffney, M. Gatu Johnson, V. GLE-

BOV, V. N. Goncharov, G. P. Grim, E. Hartouni, R. Hatarik, D. E. Hinkel, L. B. Hopkins, I. Igumenshchev, P. Knapp, J. P. Knauer, A. L. Kritcher, O. Landen, A. Pak, S. Le Pape, T. Ma, A. G. MacPhee, D. H. Munro, R. C. Nora, P. K. Patel, L. Peterson, P. B. Radha, S. P. Regan, H. Rinderknecht, C. Sangster, B. K. Spears, and C. Stoeckl, Nuclear Fusion **59**, 032009 (2018).

[48] O. A. Hurricane, P. T. Springer, P. K. Patel, D. A. Callahan, K. Baker, D. T. Casey, L. Divol, T. Doppner, D. E. Hinkel, M. Hohenberger, L. F. Berzak Hopkins, C. Jarrott, A. Kritcher, S. Le Pape, S. Maclaren, L. Masse, A. Pak, J. Ralph, C. Thomas, P. Volegov, and A. Zylstra, Physics of Plasmas **26**, 052704 (2019).

[49] L. A. Pickworth, B. A. Hammel, V. A. Smalyuk, H. F. Robey, R. Tommasini, L. R. Benedetti, L. Berzak Hopkins, D. K. Bradley, M. Dayton, S. Felker, J. E. Field, S. W. Haan, B. Haid, R. Hatarik, E. Hartouni, D. Holunga, M. Hoppe Jr., N. Izumi, S. Johnson, S. Khan, T. Kohut, B. Lahmann, O. L. Landen, S. LePape, A. G. MacPhee, E. Marley, N. B. Meezan, J. Milovich, S. R. Nagel, A. Nikroo, A. Pak, R. Petrasso, B. A. Remington, N. G. Rice, H. A. Scott, P. T. Springer, M. Stadermann, C. Walters, K. Widmann, and W. W. Hsing, Physics of Plasmas **25**, 082705 (2018).

[50] A. Pak, L. Divol, C. R. Weber, L. F. B. Hopkins, D. S. Clark, E. L. Dewald, D. N. Fittinghoff, V. Geppert-Kleinrath, M. Hohenberger, S. Le Pape, T. Ma, A. G. MacPhee, D. A. Mariscal, E. Marley, A. S. Moore, L. A. Pickworth, P. L. Volegov, C. Wilde, O. A. Hurricane, and P. K. Patel, Physical Review Letters **124**, 145001 (2020).

[51] J. A. Frenje, T. J. Hilsabeck, C. W. Wink, P. Bell, R. Bionta, C. Cerjan, M. Gatu Johnson, J. D. Kilkenny, C. K. Li, F. H. Séguin, and R. D. Petrasso, Review of Scientific Instruments **87**, 11D806 (2016).

[52] S. F. Khan, L. C. Jarrott, P. K. Patel, N. Izumi, T. Ma, A. G. MacPhee, B. Hatch, O. L. Landen, J. Heinmiller, J. D. Kilkenny, and D. K. Bradley, Review of Scientific Instruments **89**, 10K117 (2018).